Materials Advances

ROYAL SOCIETY OF CHEMISTRY

PAPER

View Article Online
View Journal | View Issue

Cite this: *Mater. Adv.*, 2025, 6, 5114

Exploring metal nanocomposites for asphaltene removal: the role of Cu-BTC, $CoMn_2O_4$ and K-OMS-2 in the adsorption and oxidation of asphaltenes†

Abhishek Nayak, Shanon Viegas, Nithya Rajagopal, Adrian Marcel Rodrigues, Harshini Dasari and Nethaji Sundarabal *

Asphaltenes, the most polar and complex class of compounds in petroleum crude oils, pose significant challenges in refining processes due to their tendency to precipitate, causing fouling, clogging, and corrosion in pipelines and reactors. These issues are further increased by their solubility behaviour, making their removal difficult. The present study investigates the synthesis of metal nanocomposites focused on a metal–organic framework (Cu-BTC), a spinel oxide ($CoMn_2O_4$) and an octahedral molecular sieve (K-OMS-2) for the adsorption and oxidation of asphaltenes from model solutions. The prepared nanocomposites were characterised using FE-SEM, EDX, HR-TEM, FT-IR, XRD, and BET surface area analysis. Furthermore, they were tested for their ability to adsorb asphaltenes using batch adsorption studies, and the equilibrium data obtained were interpreted using Langmuir, Freundlich, Temkin, Redlich–Peterson, and Hill isotherm models. Thermodynamic studies were performed, and changes in enthalpy (ΔH^0), entropy (ΔS^0) and free energy (ΔG^0) were determined from the data. Kinetic studies were conducted, and the data were analysed using pseudo-first-order (PFO), pseudo-second-order (PSO), Elovich, intraparticle diffusion, and Boyd diffusion models. Adsorption studies revealed that asphaltenes' adsorption onto Cu-BTC was best explained by the Freundlich adsorption isotherm, while $CoMn_2O_4$ followed the Langmuir model and K-OMS-2 was governed by the Hill isotherm. The monolayer adsorption capacities of the prepared nanocomposites varied in the order: K-OMS-2 (245 mg g^{-1}) > $CoMn_2O_4$ (77 mg g^{-1}) > Cu-BTC (50 mg g^{-1}). Kinetic studies indicated that the adsorption process was rapid, and the Boyd diffusion model suggested that the rate-limiting step was the external mass transfer of asphaltenes onto the adsorbent. $CoMn_2O_4$ exhibited the highest catalytic activity among the prepared nanocomposites for asphaltene oxidation, achieving a 140 °C reduction in oxidation temperature. The findings indicated that K-OMS-2 is an effective material for adsorption, while $CoMn_2O_4$ is efficient in the catalytic oxidation of asphaltenes.

Received 7th February 2025,
Accepted 13th June 2025

DOI: 10.1039/d5ma00106d

rsc.li/materials-advances

1 Introduction

Asphaltenes are a high molecular weight class of compounds in crude oil, known for their limited solubility in aromatic solvents and complete insolubility in aliphatic solvents.[1] Due to their complex molecular nature, asphaltenes have posed significant challenges in the petroleum industry, often leading to flow assurance issues as illustrated in Fig. 1. In their soluble state, asphaltenes increase the molecular weight of crude oil, raising the crude viscosity by as much as 750-fold.[2] When they precipitate, they form scales that reduce the flow area and can cause severe corrosion. The presence of asphaltenes in crude oil incurs significant expenditure for petroleum industries towards their removal. Furthermore, asphaltenes have no practical applications and are considered solid waste, which adds to the costs associated with handling, storage, and disposal.[3] Therefore, it is essential to implement effective strategies for their removal and management to reduce their adverse effects.

The interference of asphaltenes can be observed at every stage of petroleum production, transport and refining. Several removal strategies are employed to mitigate these adverse effects, including reservoir precipitation modelling, asphaltene precipitation simulations, chemical inhibition of asphaltenes, mechanical scraping, pigging, solvent extraction, coking, and adsorption.[4] Modelling and simulation serve as preventive strategies for asphaltenes interference; however, they are

Department of Chemical Engineering, Manipal Institute of Technology, Manipal Academy of Higher Education, Manipal, India. E-mail: nethaji.s@manipal.edu; Tel: +91 0820 2924316

† Electronic supplementary information (ESI) available. See DOI: https://doi.org/10.1039/d5ma00106d

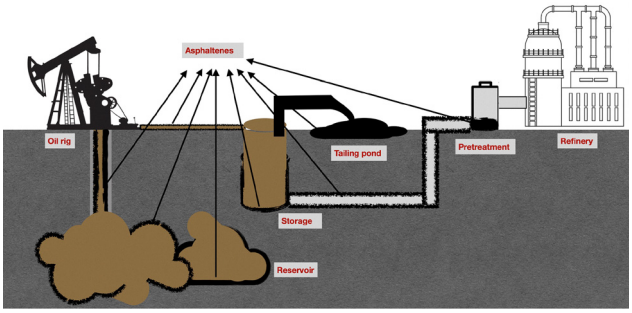

Fig. 1 Asphaltene interference in petroleum industries.

inherently complex, well-specific, and demand expert knowledge. Chemical inhibition is an effective preventive measure that depends on the use of expensive chemical additives. Maintenance methods such as scraping, pigging, and solvent extraction are labour-intensive, costly, and lead to substantial operational downtime. Coking facilitates the conversion of asphaltenes into valuable products, which offers added value. Among these techniques, adsorption has shown considerable promise due to high removal efficiency and operational simplicity; nonetheless, it still requires optimisation for large-scale applications.[5] As asphaltenes are a highly polar class of compounds, charged interactions strongly influence their adsorption. However, these stable charged interactions can lead to secondary pollution.[6] To address this, the oxidation of asphaltenes is explored for the regeneration of the adsorbent, enabling reusability and reducing solid waste.

Various materials, such as carbon composites,[7] metal composites,[8] and metal oxide composites,[9] have been explored for the adsorption and oxidation of asphaltenes. Among these, transition metal composites are particularly studied due to their ability to exhibit multiple oxidation states, provide diverse surface functionalities, and display various morphologies.[10] The effects of metal oxide morphology are well established in applications such as oxidation catalysts for various processes. However, the influence of metal composite morphology on adsorption and oxidation has not been studied extensively. As a result, mixed-metal oxides, metal–organic frameworks (MOFs), and octahedral molecular sieves (OMS), which are known adsorbents and oxidation catalysts, remain to be investigated for asphaltene removal and oxidation.

MOFs are porous crystalline materials formed by linking metal ions with organic linkers. They are well known for their high surface area, porosity, and tunable properties.[11] These materials have been studied extensively for applications involving gas storage and gas separation,[12–17] as well as for adsorption, owing to their excellent surface properties. MOFs demonstrate significant potential in various adsorption applications, particularly in the adsorption of ionic compounds.[18–20] Additionally, MOFs possess limited catalytic activity, often restricted to gas-phase reactions. Despite their proven adsorption and oxidation potential, MOFs have not been thoroughly explored for asphaltene adsorption. Therefore, this study investigates the use of MOFs for the adsorption and oxidation of asphaltenes.

Mixed metal oxides are compounds consisting of two metals in the form $A_xB_yO_z$.[21] These oxides occur naturally in the form of mineral rocks and gemstones, while various phases of mixed metal oxides are synthesised and studied for diverse applications.[22] Generally, mixed metal oxides with spinel, rutile, haematite, ilmenite and perovskite crystal structures are widely used in numerous applications.[1,23–29] Among them, spinel oxides are exceptionally versatile and have applications in supercapacitors,[30] photocatalysis,[31] oxidation catalysis,[32] battery electrode materials,[33] electrocatalysis,[34] and adsorption.[35,36] Spinel oxides have a structure where large metal cations are bound to smaller cations and oxygen, represented by the formula AB_2O_4.[37] The cations are coordinately bound by tetrahedrally bound A, octahedrally bound B and an oxygen atom. Spinels are often used as catalysts due to their multiple oxidation states.[38] Despite their proven adsorption and catalytic properties, they are yet to be explored for the adsorption and oxidation of asphaltenes.

OMS are inorganic materials widely known for their octahedrally bound three-dimensional structure.[39] OMS possess a porous surface with a tunnel-like three-dimensional framework, making them suitable for molecular separation and catalysis applications.[40] They are generally used in ion exchange,[40] separation processes,[41] catalysis,[42] and adsorption.[43] OMS consist of metal oxide molecules octahedrally bound by coordinate bonds, with transition metal oxides such as manganese forming the core of the octahedra surrounded by oxygen atoms. These octahedral units link together to form a tunnel structure, characteristic of OMS. However, the OMS's size and shape depend on the arrangement of the metal–oxygen octahedra.[44] Among the OMS, OMS-2 (cryptomelane) is well known for its 2×2 tunnel structure and has the general formula $A_xMn_8O_{16}$, where A is potassium, sodium, hydrogen or transition metals.[45] OMS-2 is widely used for adsorption, oxidation catalysis, and environmental remediation applications. Although OMS materials are well-known for their effective adsorption and catalytic abilities, their potential for asphaltene removal and oxidation has not been investigated.

Hence, in the present work, multifunctional materials, namely, Cu-BTC, $CoMn_2O_4$, and K-OMS-2, were investigated for the adsorption and oxidation of asphaltenes. The study evaluates structurally and functionally diverse materials for asphaltene treatment, a comparative approach that has not been previously reported. The distinct properties of each material are strategically explored: K-OMS-2 for its structural characteristics and redox catalytic activity,[46,47] $CoMn_2O_4$ for its acid–base surface characteristics,[48] and Cu-BTC for its highly porous and functionalised framework. This work aims to elucidate how these differing characteristics influence the adsorption and oxidation behaviour of asphaltenes.

2 Experiments

2.1 Chemicals and materials

The reagents used in the work were *n*-heptane (C_7H_{16}, 99%), toluene ($C_6H_5CH_3$, 99.5%), xylene (C_8H_{10}, 99.5%), and potassium manganate(VII) ($KMnO_4$, 99%) obtained from Loba Chemie, India. *N*,*N*-Dimethylformamide (DMF, $HCON(CH_3)_2$, 99.9%), copper(II)

nitrate trihydrate ($Cu(NO_3)_2{\cdot}3H_2O$, 99%), cobalt(II) nitrate hexahydrate ($Co(NO_3)_2{\cdot}6H_2O$, 98%), manganese(II) nitrate hexahydrate ($Mn(NO_3)_2{\cdot}6H_2O$, 98%), manganese(II) sulphate monohydrate ($MnSO_4{\cdot}H_2O$, 99%), nitric acid (HNO_3, 69%), and ammonium hydroxide (NH_4OH, 30%) were supplied by Merck, India. Ethanol (C_2H_5OH, 100%) was procured from Hayman, UK, benzene-1,3,5-tricarboxylic acid (BTC, $C_9H_6O_6$, 95%) was provided by Sigma-Aldrich, USA and bitumen (VG 80-100) was sourced from Shell, India. All chemicals were used as received without further purification.

2.2 Preparation of nanocomposites for adsorption of asphaltenes

The following nanocomposites were prepared and studied for their adsorption and oxidation characteristics.

2.2.1 Preparation of Cu-BTC. Cu-BTC was synthesised using a solvothermal process. 0.8 g copper nitrate and 0.7 g BTC were dissolved in ethanol. The solution was charged to a 100 mL Teflon-lined autoclave and kept at 120 °C for 12 hours.[49] The sample was then washed with DMF, ethanol and distilled water and dried at 90 °C. The sample was then stored in a desiccator for future use.

2.2.2 Preparation of $CoMn_2O_4$. $CoMn_2O_4$ was prepared using the co-precipitation method. 25 mL of 0.2 M cobalt nitrate and 50 mL of 0.2 M manganese nitrate were mixed, and the resulting solution was reduced using ammonium hydroxide solution. The ammonium hydroxide solution was added dropwise until the solution reached pH 10, and the mixture was stirred vigorously. The resulting solid precipitate was separated and washed to remove residual chemicals. The solid was then calcined at 650 °C for 4 hours, and the obtained $CoMn_2O_4$ was stored in a desiccator for further use.[50]

2.2.3 Preparation of K-OMS-2. The K-OMS-2 nanocomposite for asphaltene adsorption was prepared using reflux boiling. 5 g of potassium permanganate and 7.5 g of manganese sulphate were added to 100 mL distilled water and mixed thoroughly. 3 mL of concentrated nitric acid was mixed with the solution and transferred to a round-bottom flask with a reflux setup attachment. The solution was then boiled under reflux for 24 hours, and the resulting precipitate was separated. The precipitate was then washed until residual precursors were completely removed. The washed precipitate was calcined at 500 °C for 4 hours,[51] and the resulting material was stored in a desiccator.

2.3 Characterisation of the prepared metal nanocomposites

The prepared nanocomposites were characterised using BET, XRD, FT-IR, FE-SEM, EDX, and HR-TEM. The surface area analysis was performed in a Smart sorb 92/93 instrument using the BET adsorption model. XRD of the prepared materials was carried out in a Rigaku Miniflex 600 (5^{th} gen). The FE-SEM and EDX analyses were carried out in a Carl Zeiss ULTRA 55 instrument, and FT-IR analysis was performed using a Shimadzu-8400S. The HR-TEM imaging was obtained using a JEOL Japan, JEM-2100 Plus.

2.4 Extraction of asphaltenes from bitumen

Asphaltenes were extracted from bitumen using *n*-heptane in a ratio of 1 : 40 (1 part bitumen : 40 parts *n*-heptane, ASTM D2007-80).[52] The mixture of bitumen and *n*-heptane was stirred for 24 hours at room temperature and sonicated for an hour. The asphaltenes form a solid precipitate, which was filtered using filter paper and separated from the solution. The wet asphaltenes were dried for 24 hours and stored in an airtight container. The asphaltene model solution was prepared by diluting asphaltenes in toluene and utilised in adsorption studies.[53]

The *n*-heptane was recovered from *n*-heptane-bitumen solution *via* distillation using a round-bottom flask connected to a condenser. The spent solution was boiled at 98 °C, and the resulting colourless *n*-heptane distillate fraction was collected and reused in subsequent extraction.

2.5 Asphaltene adsorption studies using the prepared metal nanocomposites

Adsorption studies of asphaltenes using metal nanocomposites were conducted with working solutions prepared by diluting the asphaltene model solution in toluene. The asphaltene adsorption studies included the effect of nanocomposite dosage, initial asphaltene concentration, thermodynamic studies and kinetic studies. The residual asphaltene solution and adsorbent were separated *via* centrifugation, and the residual asphaltene concentration was estimated at 800 nm,[54] using a Shimadzu/UV 1800 Series UV-visible spectrophotometer.

2.6 Oxidation studies of the asphaltenes over the prepared metal nanocomposites

The oxidation of asphaltenes and nanocomposite-catalysed oxidation of asphaltenes were studied using thermogravimetric analysis (TGA). The TGA analysis was carried out in a TA 55 Discovery instrument (TA instruments) with an air atmosphere maintained in the furnace. The oxidation was carried out over 50 °C to 700 °C, during which the weight loss and derivative weight loss were recorded.[55]

3 Results and discussion

3.1 Characterisation of the prepared metal nanocomposites

The prepared metal nanocomposites were characterised using FE-SEM, HR-TEM, EDX, BET, XRD, and FT-IR. Surface imaging, morphology, and particle size of the prepared nanocomposites were assessed using FE-SEM and HR-TEM. The obtained micrographs are depicted in Fig. 2 and 3. Fig. 2A and B show the micrographs of Cu-BTC obtained at 10k× and 75k× magnifications. The Cu-BTC particles exhibit octahedral morphology, consistent with observations reported by Cheng *et al.*[56] At a magnification of 75k×, a porous structure in the range of 100 nm with slit-like openings was observed on the octahedral surface. Similarly, HR-TEM micrographs in Fig. 3A and B reveal the crystalline phases of the octahedral Cu-BTC. The crystals were well defined and the particle size of the crystal was about 55 nm.[57] The FE-SEM micrographs of $CoMn_2O_4$, shown in Fig. 2C and D, depict the formation of spherical particle clusters. The magnified micrographs showed that these particles exhibited a spherical-like morphology with an average

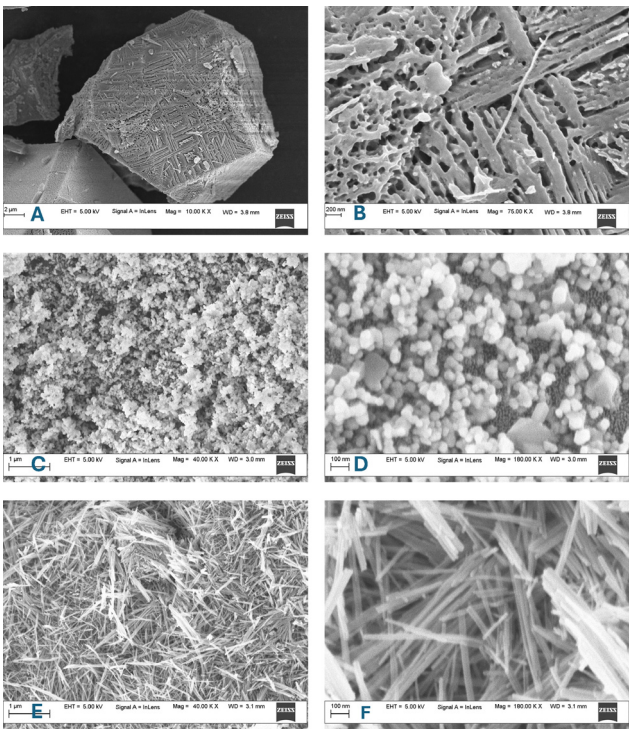

Fig. 2 FE-SEM micrographs of (A) Cu-BTC at 10k×, (B) Cu-BTC at 75k×, (C) $CoMn_2O_4$ at 40k×, (D) $CoMn_2O_4$ at 180k×, (E) K-OMS-2 at 40k×, and (F) K-OMS-2 at 180k×.

diameter of 45 nm.[58] However, HR-TEM micrographs shown in Fig. 3C and D revealed an elongated spherical structure.[59] Similarly, Fig. 2E and F depict the FE-SEM micrographs of K-OMS-2, which displayed a fibre-like morphology. The fibrils were observed to be distributed uniformly.[60] The fibre morphology was confirmed by HR-TEM depicted in Fig. 3E and F, where the width of the fibril was found to be about 30 nm.[61] The FE-SEM of the nanocomposites after asphaltene adsorption was performed, and the obtained micrographs of the nanocomposites are depicted in Fig. 4. This technique was employed to ensure the structural stability of the nanocomposites. From the micrographs, the octahedral structure of Cu-BTC, elongated spherical-like structure of $CoMn_2O_4$, and fibre-like structure of K-OMS-2 were retained after adsorption.

The EDX analysis of the prepared metal nanocomposites was conducted before and after asphaltene adsorption to confirm the successful uptake of asphaltenes. The obtained spectrum is shown in Fig. S1 and S2 (ESI†). The EDX spectra confirmed the purity and elemental composition of the prepared metal nanocomposites. The spectrum in Fig. S1A (ESI†) confirmed the presence of Cu originating from the metal component, and C and O derived from the organic component in the prepared Cu-BTC. The EDX spectra of $CoMn_2O_4$ in Fig. S1B (ESI†) confirmed the presence of Co, Mn, and O. Similarly, the presence of K, Mn and O in K-OMS-2 was confirmed from the EDX spectra in Fig. S1C (ESI†) with no detectable impurities. Fig. S2 (ESI†) confirmed asphaltene uptake by indicating the presence of carbon in the EDX spectra of the spent nanocomposites.

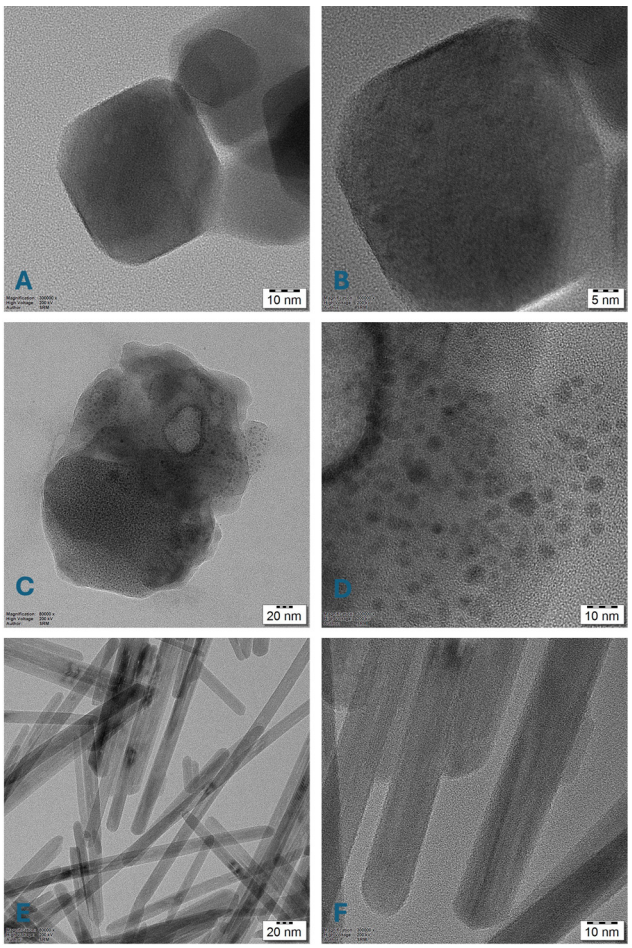

Fig. 3 HR-TEM images of (A) Cu-BTC at 300k×, (B) Cu-BTC at 500k×, (C) $CoMn_2O_4$ at 80k×, (D) $CoMn_2O_4$ at 300k×, (E) K-OMS-2 at 80k×, and (F) K-OMS-2 at 300k×.

FT-IR analysis of the prepared metal nanocomposites was performed to determine the surface functional moieties. The spectrum was obtained for the nanocomposites before and

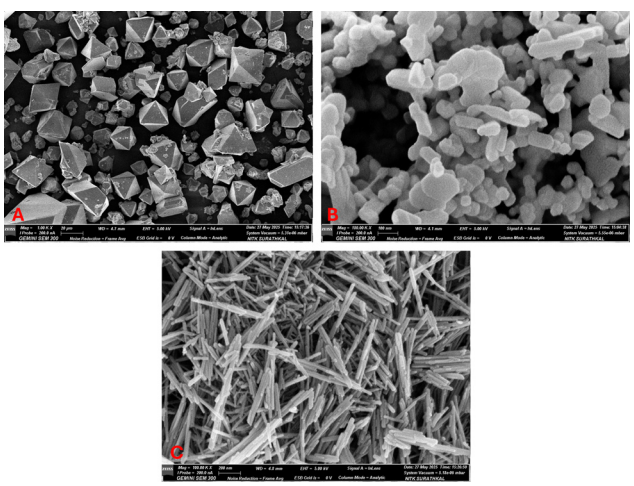

Fig. 4 FE-SEM micrographs of (A) Cu-BTC, (B) $CoMn_2O_4$, and (C) K-OMS-2 after asphaltene adsorption.

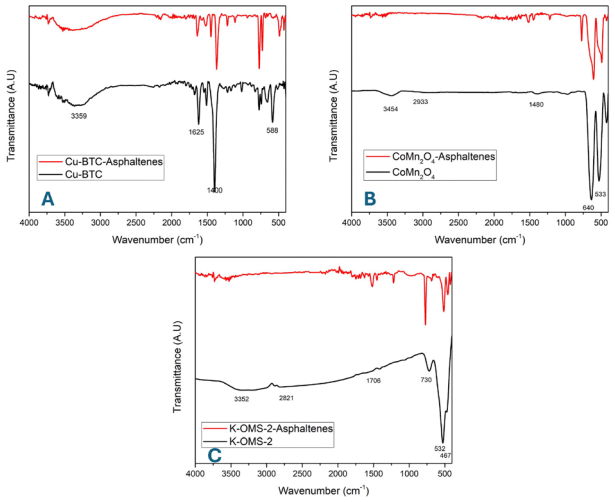

Fig. 5 FT-IR spectrum of (A) Cu-BTC, (B) $CoMn_2O_4$, and (C) K-OMS-2, before and after asphaltene adsorption.

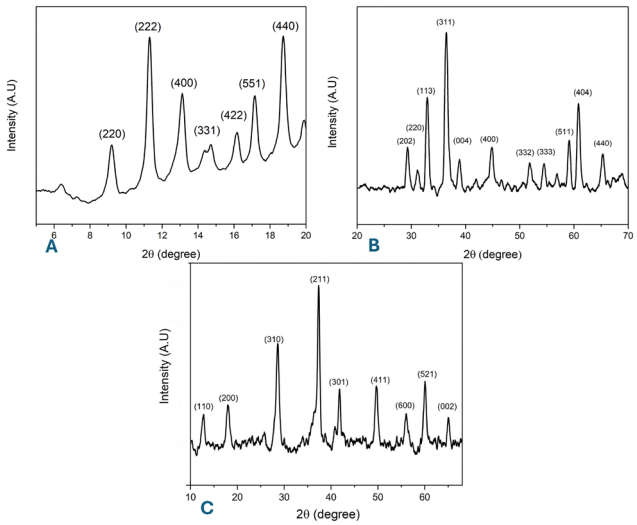

Fig. 6 XRD spectrum of (A) Cu-BTC, (B) $CoMn_2O_4$, and (C) K-OMS-2.

after asphaltene adsorption, as shown in Fig. 5. The surface functional groups of the adsorbent play a vital role in determining the mechanism of adsorption, particularly when the adsorbate contains charged functional groups. From the FT-IR spectrum shown in Fig. 5A, the transmittance peaks representing C═O, C–O and Cu–O were observed at 1625 cm^{-1}, 1400 cm^{-1} and 588 cm^{-1}, which are characteristic peaks of Cu-BTC.[62] In the FT-IR spectrum of Cu-BTC post-asphaltene adsorption, the Cu–O bond peak exhibited a significant shift alongside reduced intensity in the characteristic peaks, confirming asphaltene adsorption. The FT-IR spectrum of the prepared $CoMn_2O_4$ is represented by Fig. 5B. $CoMn_2O_4$ was confirmed by the absorption peak corresponding to the vibration of Co–O coordination and Mn–O coordination bond vibrations, which was observed at 640 cm^{-1} and 533 cm^{-1}, respectively.[63,64] A reduction in the intensity of the characteristic peaks was observed, in addition to a shift towards a lower wavenumber, which indicated asphaltenes' accumulation on the surface. Similarly, the FT-IR spectrum for the prepared K-OMS-2 was obtained, as shown in Fig. 5C. The bands representing K-OMS-2 were observed at 467 cm^{-1}, 532 cm^{-1}, and 730 cm^{-1}. The observed characteristic peak represents vibrations of the Mn–O units of the octahedral manganese oxide.[65] Furthermore, O–H stretching of water was observed in the higher wavenumber region, which confirmed the moisture in the material. The presence of the moisture could be from the atmosphere or the hygroscopic nature of the prepared metal nanocomposites. After the asphaltene uptake, the peaks representing K-OMS-2 were observed to reduce in intensity. Furthermore, new peaks in the 1200–1600 cm^{-1} region were identified, indicating possible C═O/C═N stretching from asphaltene molecules.

The prepared metal nanocomposites were further characterised for the surface area using BET analysis. A high surface area of 433 m^2 g^{-1} and 400 m^2 g^{-1} was observed for Cu-BTC and K-OMS-2, respectively. However, in the case of $CoMn_2O_4$, a lower surface area of 5 m^2 g^{-1} was observed. The high surface area observed in Cu-BTC could be attributed to void spaces and the porous structures, while the fibre-like structure could have contributed towards high surface area in K-OMS-2. The low surface area of $CoMn_2O_4$ may be the result of particle agglomeration.

XRD spectra of the prepared metal nanocomposites are depicted in Fig. 6. From Fig. 6A, the XRD spectrum of Cu-BTC showed peaks representing (220), (400), (331), (422), (511), and (440) planes at 9.5°, 13.8°, 14.9°, 16.9°, 17.5°, and 19.1°, respectively. These peaks confirmed the face-centred cubic crystal lattice of Cu-BTC. The identified XRD peaks were consistent with the peaks in ICDD standard data, ICDD pdf number 00-062-1183.[56]

From Fig. 6B, peaks corresponding to the (202), (220), (113), (311), (004), (400), (332), (333), (511), (404), and (440) planes were identified at 29.4°, 31.2°, 33°, 36.5°, 39°, 45°, 52°, 54.5°, 59.2°, 60.8°, and 65.5°, respectively. The spectrum confirmed the body-centred tetragonal phase of $CoMn_2O_4$, matching JCPDS no. 18-0408.[66,67]

The XRD spectrum of K-OMS-2 shown in Fig. 6C exhibited peaks for planes (110), (200), (310), (211), (301), (411), (600), (521), and (002) at 12.5°, 17.5°, 28°, 37°, 42°, 50°, 56°, 60.5°, and 65.5°. The identified peaks confirmed the tetragonal crystalline structure of K-OMS-2, which was consistent with JCPDS: 29-1020 that represents cryptomelane.[60]

Further surface characteristics, such as acidic and basic functional groups, were determined by Boehm titration.[68] The titration results revealed basic functional group contents of 0.60 mmol g^{-1}, 0.96 mmol g^{-1}, and 0.40 mmol g^{-1}, and acidic functional group contents of 1.00 mmol g^{-1}, 0.86 mmol g^{-1}, and 1.14 mmol g^{-1}, for Cu-BTC, $CoMn_2O_4$, and K-OMS-2, respectively.

3.2 Batch adsorption studies

A stock of asphaltene model solution was prepared in toluene, with 1 g of asphaltenes completely dissolved in 1 litre of toluene. The required concentrations of the working solution

were prepared by diluting the stock solution. Batch adsorption studies were conducted using the prepared metal nanocomposite as the adsorbent and the working solution as the adsorbate. The batch adsorption studies included the effect of adsorbent dosage and the effect of initial asphaltene concentration, as well as kinetic and thermodynamic studies. Furthermore, the recyclability of the spent adsorbent was assessed by desorbing the adsorbed asphaltenes. The residual asphaltene concentration from the adsorption studies was estimated using a UV-visible spectrophotometer. The estimation was carried out with reference to toluene in the reference cell.

The metal nanocomposites were used in the study of the effect of adsorbent dosage, which included varying the nanocomposite dosage from 2.5 g L^{-1} to 25 g L^{-1}. The experiments were carried out at 30 °C, 150 rpm and 24 hours contact time, with an asphaltene concentration of 250 mg L^{-1} and the resulting relationship is depicted in Fig. S3 (ESI†). From Fig. S3A (ESI†), a 95% removal was achieved with the Cu-BTC dosage of 25 g L^{-1}. However, a dosage of 12.5 g L^{-1} proved to be effective, since the asphaltene adsorption is observed to be 95%, and the removal appeared to saturate as the dosage was increased beyond 12.5 g L^{-1}. Similar behaviour was observed for $CoMn_2O_4$, as depicted in Fig. S3B (ESI†). From Fig. S3C (ESI†), the removal of asphaltenes was found to increase with increasing dosage for dosages below 20 g L^{-1}. However, the adsorption percentage remained constant for dosages above 20 g L^{-1}, indicating saturation of the adsorbent's active sites.

Asphaltene adsorption using metal nanocomposites was evaluated for the effect of initial asphaltene concentration, and the adsorption behaviour is shown in Fig. S4 (ESI†). The studies were conducted by varying the initial asphaltene concentration from 100 mg L^{-1} to 1000 mg L^{-1}, while keeping the adsorbent dosage constant (12.5 g L^{-1} for Cu-BTC and $CoMn_2O_4$, 20 g L^{-1} for K-OMS-2). The experiments were performed at 30 °C, with a stirring speed of 150 rpm, for 24 hours. From the figure, the adsorption percentage was found to decrease with increasing initial asphaltene concentration across all prepared materials. Maximum adsorption occurred at an asphaltene concentration of 100 mg L^{-1}. The increase in asphaltene concentration led to a reduction in adsorption percentage, likely due to a decrease in available active sites.

3.2.1 Isotherm studies of asphaltene adsorption onto the prepared metal nanocomposites. The equilibrium data from the batch adsorption studies of asphaltenes were interpreted using five adsorption isotherms, namely, Langmuir, Freundlich, Temkin, Redlich–Peterson, and Hill adsorption isotherm models given in eqn (1), (2), (3), (4) and (5), respectively.

The Langmuir isotherm model is given by:[69]

$$q_e = \frac{q_m \cdot K_L \cdot C_e}{1 + K_L \cdot C_e} \quad (1)$$

where C_e is equilibrium adsorbate concentration (mg L^{-1}), K_L is the Langmuir coefficient (L mg^{-1}), and q_e is the equilibrium adsorption capacity (mg g^{-1}).

The Freundlich isotherm model is given by:[69]

$$q_e = K_F \cdot C_e^{(1/n_F)} \quad (2)$$

K_F is the Freundlich coefficient (mg g^{-1}), which represents the adhesion ability of the adsorbate onto the adsorbent and n_F is the degree of nonlinearity between adsorption and solution concentration.

The Temkin isotherm model is given by:[70]

$$q_e = \frac{R \cdot T}{b_T} \ln(K_T \cdot C_e) \quad (3)$$

b_T is the heat of adsorption (J mol^{-1}), T is the absolute temperature (K), R is the gas constant (8.314 J mol^{-1} K^{-1}) and K_T is the equilibrium binding constant (L mg^{-1}).

The Redlich–Peterson isotherm model is given by:[71]

$$q_e = \frac{K_{RP} \cdot C_e}{1 + \alpha_{RP} \cdot C_e^{\beta_{RP}}} \quad (4)$$

K_{RP} is the Redlich–Peterson coefficient (L g^{-1}), α_{RP} is a constant (L mg^{-1}), and β_{RP} is the exponent.

The Hill isotherm model is given by:[72]

$$q_e = \frac{q_m \cdot C_e^{n_H}}{1 + K_D \cdot C_e^{n_H}} \quad (5)$$

n_H is the Hill coefficient and K_D is the dissociation constant (mg L^{-1}).

The isotherm model fitting for the asphaltene adsorption equilibrium data is depicted in Fig. 7, with model parameters tabulated in Table 1. Adsorption of asphaltenes onto Cu-BTC, $CoMn_2O_4$, and K-OMS-2 is shown in Fig. 7A, B and C, respectively. The model fitting was evaluated by using the χ^2 value and r^2 values, where the r^2 value indicates the goodness of the fit, and χ^2 quantifies the deviation of the experimental values from the model predictions. Since the r^2 values were close, the goodness of fit was determined by χ^2. The asphaltene adsorption using Cu-BTC was found to be governed by the Freundlich isotherm since the χ^2 value is the least for this model. The Freundlich isotherm indicates a possible multilayer adsorption on heterogeneous adsorption sites of the adsorbent, and since $n_F \gg 1$, the adsorption is favourable. The $CoMn_2O_4$ system was found to follow the Langmuir isotherm model. The model describes adsorption processes in which adsorbate molecules form a monolayer on homogeneous adsorption sites. The χ^2 for the Langmuir model fitting was found to be the lowest for the $CoMn_2O_4$ system; hence, the adsorption is likely to be monolayer in nature.[73] Similarly, the adsorption of asphaltenes using K-OMS-2 was found to be explained by the Hill isotherm model. The Hill model describes cooperative adsorption in the system. According to the model parameters, asphaltenes' adsorption promotes cooperative adsorption, thereby enhancing the uptake. The Langmuir isotherm parameters also provided the maximum monolayer adsorption capacity (q_m) of the materials, and the q_m was in the order K-OMS-2 (245.79 mg g^{-1}) > $CoMn_2O_4$ (77.04 mg g^{-1}) > Cu-BTC (50.59 mg g^{-1}). The adsorption was strongly influenced by the surface acidity and basicity of the adsorbents. Among the materials, K-OMS-2

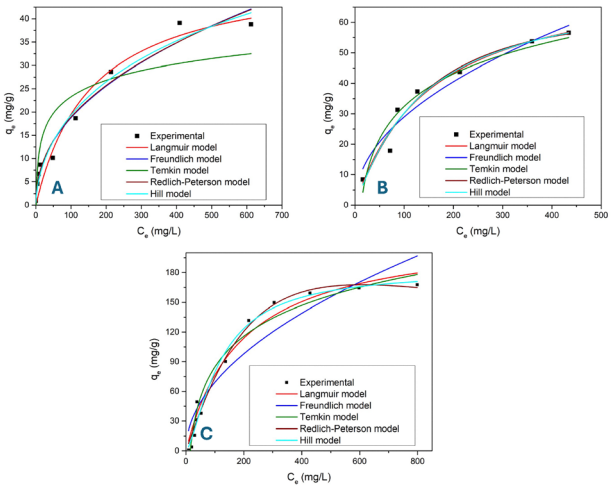

Fig. 7 Isotherm plots for the adsorption of asphaltenes onto (A) Cu-BTC (adsorbent dosage = 12.5 g L^{-1}, t = 24 h, T = 30 °C, 150 rpm), (B) $CoMn_2O_4$ (adsorbent dosage = 12.5 g L^{-1}, t = 24 h, T = 30 °C, 150 rpm), and (C) K-OMS-2 (adsorbent dosage = 20 g L^{-1}, t = 24 h, T = 30 °C, 150 rpm).

Table 1 Isotherm model parameters for asphaltene adsorption onto the metal nanocomposites

Adsorption model	Parameter	Cu-BTC	$CoMn_2O_4$	K-OMS-2
Langmuir	q_m (mg g^{-1})	50.590	77.040	245.790
	K_L (L mg^{-1})	0.006	0.006	0.007
	r^2	0.980	0.968	0.986
	χ^2	9.756	12.684	140.841
Freundlich	K_F (mg g^{-1})	2.399	3.110	10.310
	n_F	2.239	2.060	2.250
	r^2	0.956	0.923	0.939
	χ^2	6.593	21.674	479.178
Temkin	K_T (L mg^{-1})	0.959	0.082	0.065
	b (J mol^{-1})	494.155	164.018	56.054
	r^2	0.760	0.929	0.956
	χ^2	52.022	22.442	198.896
Redlich–Peterson	K_{RP} (L g^{-1})	9.352	0.436	0.838
	α_{RP} (L mg^{-1})	3.573	0.002	1.45×10^{-4}
	β_{RP}	0.566	1.138	1.489
	r^2	0.964	0.951	0.982
	χ^2	7.657	15.526	79.440
Hill	q_m (mg g^{-1})	106.946	73.162	181.752
	K_D (mg L^{-1})	65.335	197.275	1010.827
	n_H	0.579	1.071	1.447
	r^2	0.968	0.950	0.982
	χ^2	6.878	15.725	79.202

exhibited the highest acidity, leading to its maximum adsorption capacity.[74] The q_m for asphaltene adsorption onto K-OMS-2 was found to be one of the highest values reported in the literature.

3.3 Adsorption kinetics studies of asphaltene adsorption onto metal nanocomposites

Time-dependent adsorption experiments were conducted to investigate the adsorption of asphaltenes onto the prepared metal nanocomposites, and kinetic models were used to study the adsorption phenomenon. The asphaltene solution concentration was fixed at 500 mg L^{-1}, the adsorbent dosage was fixed at 6.25 g L^{-1}, and the kinetic data were recorded. The resulting asphaltene uptake with time is depicted in Fig. S5 (ESI†).

From Fig. S5A (ESI†), the adsorption of asphaltenes using Cu-BTC attained equilibrium in 0.6 h. Similarly, Fig. S5B (ESI†) shows that the equilibrium for asphaltene adsorption onto $CoMn_2O_4$ was observed at about 6 h of contact time, while equilibrium was attained in 2.5 h for K-OMS-2 (Fig. S5C, ESI†). The time-dependence experimental data were further interpreted using widely applied kinetic models: the PFO (eqn (6)), PSO (eqn (7)), and Elovich (eqn (8)) adsorption kinetic models.

The PFO model equation is given by,[75]

$$q_t = q_e \cdot (1 - e^{-k_1 \cdot t}) \quad (6)$$

where q_t is adsorption capacity at time t (mg g^{-1}), and k_1 is PFO coefficient (h^{-1}).

The PSO kinetic model equation is given as,[75]

$$q_t = \frac{k_2 \cdot q_e^2 \cdot t}{1 + k_2 \cdot q_e \cdot t} \quad (7)$$

where k_2 is the PSO rate constant (g mg^{-1} h^{-1}).

The Elovich kinetic model equation is given as,[76]

$$q_t = \frac{1}{\beta} \ln(\alpha_E \cdot \beta_E \cdot t + 1) \quad (8)$$

where α_E is the initial adsorption rate (mg g^{-1} min^{-1}) and β_E is the desorption constant (g mg^{-1}).

The kinetic model plots for asphaltene adsorption onto the prepared metal nanocomposite are shown in Fig. S6 (ESI†). The kinetic studies of asphaltene adsorption onto Cu-BTC, $CoMn_2O_4$, and K-OMS-2 are represented in Fig. S6A, B, and C (ESI†), respectively, and the model parameters are given in Table 2. The adsorption of asphaltenes by Cu-BTC was observed to follow the PFO model. The model suggests a possible physisorption, which could be due to the porous nature of Cu-BTC. The adsorption of asphaltenes onto $CoMn_2O_4$ was explained by the PSO model. The PSO model describes chemisorption-driven adsorption, and its fitting signifies a possible chemisorption mechanism.[77] Similarly, asphaltene adsorption using K-OMS-2 was found to be governed by the Elovich model. The Elovich model is applicable for adsorption

Table 2 Kinetic model parameters for asphaltene adsorption onto metal nanocomposites

	PFO model				PSO model				Elovich model			
Adsorbent	q_e (mg g^{-1})	k_1 (h^{-1})	r^2	χ^2	q_e (mg g^{-1})	k_2 (g mg^{-1} h^{-1})	r^2	χ^2	α_E (mg g^{-1} min^{-1})	β_E (g mg^{-1})	r^2	χ^2
Cu-BDC	6.468	16.805	0.945	0.185	7.117	3.419	0.903	0.330	120.265	0.938	0.823	0.606
$CoMn_2O_4$	34.107	1.157	0.929	10.815	38.963	0.036	0.938	9.561	1024.742	0.127	0.936	9.734
K-OMS-2	141.620	15.701	0.758	335.897	150.846	0.157	0.894	147.238	36 317.740	0.053	0.995	5.890

systems involving heterogeneous surfaces with chemisorption-driven interactions. The kinetic model parameters were analysed to determine the adsorption characteristics. The k_1 and k_2 values represent the rate of initial adsorption and driving force, respectively. These values were found to be higher for Cu-BTC, indicating rapid adsorption of asphaltenes onto Cu-BTC, a phenomenon which was also evident from the kinetic data. In addition, β_E represents the extent of adsorption, which was found to be maximum for Cu-BTC. The observation could be attributed to the physisorption of asphaltenes onto Cu-BTC, as suggested by PFO models. The α_E parameter denotes the chemisorption rate, which was found to be maximum for K-OMS-2.[78] Asphaltenes are a highly polar class of compounds, with polarity arising from charged end functional groups. Therefore, chemisorption is expected. Both kinetic and adsorption isotherm studies support this mechanism.[79] The predicted q_e values from the fitted kinetic models were found to closely match the experimental q_e values.

3.4 Mechanism of adsorption of asphaltenes onto Cu-BTC

The kinetic data were used to analyse the mechanism involved in the adsorption process. The data were analysed using the intraparticle diffusion model (eqn (9)) to investigate the adsorption mechanism, and the Boyd model (eqn (10)) was employed to determine the rate-controlling step.

The intraparticle diffusion model expression is given by,[80]

$$q_t = k_1 \cdot \sqrt{t} + C \quad (9)$$

where k_i is the intraparticle diffusion rate constant (mg g^{-1} h^{-1}), and C represents the thickness of the boundary layer.

The Boyd diffusion model equation is given as,[81]

$$B_t = -0.4977 - \ln(1 - F) \quad (10)$$

where B_t is the Boyd coefficient (dimensionless), and F is the fractional adsorption capacity.

The transport mechanism of the adsorbate towards the adsorbent was analysed using the intraparticle diffusion model, providing insights into the adsorption mechanism. The model data are represented in Fig. S7 (ESI†). Fig. S7A, B, and C (ESI†) illustrate the intraparticle diffusion model for asphaltene adsorption onto Cu-BTC, $CoMn_2O_4$, and K-OMS-2, respectively.

From the figures, the adsorption mechanism can be described using three distinct zones, namely boundary layer diffusion, intraparticle diffusion, and equilibrium stage. Boundary layer diffusion is represented by the first linear segment of the curve, and this initial phase involves asphaltene molecules migrating towards the surface of the nanocomposite. Intraparticle diffusion is explained by the subsequent linear segment, which corresponds to asphaltenes penetrating the adsorbent's pores. The equilibrium stage is the final horizontal segment that indicates saturation, where adsorption ceases due to exhausted active sites. From Fig. S7A and B (ESI†), a rapid boundary layer diffusion of asphaltenes into Cu-BTC (within 6 min) and $CoMn_2O_4$ (within 10 min) was observed, followed by intraparticle diffusion that extended for 20 min for Cu-BTC and 4 h for $CoMn_2O_4$, respectively. However, in the case of asphaltene adsorption onto K-OMS-2, a slow film diffusion process was observed, extending up to 1 h, followed by an intraparticle diffusion process that continued for up to 3 h, as shown in Fig. S7C (ESI†).[82]

The mechanism of asphaltene adsorption can be further explained by identifying the rate-limiting step. Boyd's diffusion kinetics model was employed to determine the slowest step. Boyd's diffusion plot of B_t *vs.* t is shown in Fig. S8 (ESI†). A linear line passing through the origin suggests intraparticle diffusion as the slowest step. For plots that follow a linear trend without intersecting the origin or exhibit nonlinear trends, film diffusion governs the process. However, non-linear trends with a positive intercept were observed in Boyd's plots for the asphaltene adsorption systems. Therefore, the study suggests that the adsorption process is governed by film diffusion or external mass transfer.[83] Typically, film diffusion dominates when the adsorbate has a high affinity for the adsorbent, a dilute system is used, the adsorbate particles are small, or mixing is poor.

3.5 Adsorption thermodynamic studies of asphaltene adsorption onto metal nanocomposites

The thermodynamics studies of asphaltenes adsorption using the prepared nanocomposites were conducted at 20 °C, 30 °C and 40 °C for optimised adsorbent dosage (12.5 g L^{-1} for Cu-BTC, $CoMn_2O_4$; 20 g L^{-1} for K-OMS-2) and varying asphaltene concentrations (50 mg L^{-1}, 100 mg L^{-1}, and 200 mg L^{-1}). The thermodynamic parameters, namely ΔG^0 (Gibb's free energy change, kJ mol^{-1}), ΔH^0 (enthalpy change, kJ mol^{-1}), and ΔS^0 (entropy change, J K^{-1} mol^{-1}) were calculated using the following equations:[84,85]

$$\Delta G^0 = -R \cdot T \cdot \ln(K) \quad (11)$$

K (dimensionless) is calculated as follows:[84]

$$K = K_L \cdot C_s \quad (12)$$

$$\Delta G^0 = \Delta H^0 - T \cdot \Delta S^0 \quad (13)$$

$$\ln(K) = \frac{-\Delta H^0}{R \cdot T} + \frac{\Delta S^0}{R} \quad (14)$$

where C_s is the solute concentration.

The thermodynamic parameters were calculated using K_L from isotherm plots (Fig. S9, ESI†), the van't Hoff plot (shown in Fig. S10, ESI†), and eqn (11)–(14), which are tabulated in Table 3. The change in Gibbs free energy was found to be negative for the Cu-BTC and K-OMS-2 systems, but for $CoMn_2O_4$, negative values were observed at higher temperatures. The negative values suggest a spontaneous and favourable adsorption process, with the increasing negativity at higher temperatures indicating greater favourability. Similarly, positive entropy change values indicated an increase in randomness at the solid–liquid interface during adsorption.[86] The negative enthalpy change reflects the exothermic nature of the adsorption. Values in the range of 40–800 kJ mol^{-1} represent a chemisorption-driven adsorption, while values below this range indicate physisorption.[78] However, the results imply a chemisorption-driven adsorption mechanism for $CoMn_2O_4$ and K-OMS-2, whereas Cu-BTC exhibited characteristics of physisorption. The results were consistent with the observations from the

Table 3 Thermodynamic parameters for asphaltene adsorption onto the metal nanocomposites

Adsorbent	ΔH^0 (kJ mol^{-1})	ΔS^0 (J mol^{-1})	T (K)	ΔG^0 (kJ mol^{-1})	K_L (L mg^{-1})	r^2
Cu-BTC	−22.075	128.016	293	−3.129	0.026	0.887
			303	−4.390	0.076	0.982
			313	−4.833	0.027	0.981
$CoMn_2O_4$	−46.111	47.980	293	1.688	0.036	0.999
			303	1.701	0.057	0.912
			313	−1.996	0.024	0.990
K-OMS-2	−54.799	142.132	293	−2.392	0.005	0.978
			303	−5.130	0.005	0.999
			313	−5.648	0.021	0.993

kinetic studies. In the case of asphaltene adsorption onto Cu-BTC, the mechanism follows the PFO model, which indicates physisorption, while asphaltene adsorption onto $CoMn_2O_4$ and K-OMS-2 follows the PSO and Elovich models, respectively, which represent chemisorption. The pictorial representation of the adsorption mechanism is shown in Fig. S11 (ESI†).

3.6 Adsorbent reusability studies of the spent nanocomposites

The adsorbent re-usability of the spent nanocomposites was studied for 3 regeneration cycles with a dosage of 12.5 g L^{-1} and asphaltene concentration of 250 mg L^{-1} stirred at 30 °C, 150 rpm for 24 hours. The regeneration of the spent $CoMn_2O_4$ was achieved by desorption of the adsorbed asphaltenes using xylene.[87] From the re-usability studies of the spent nanocomposites, a maximum asphaltene removal of 90%, 86%, and 77% was achieved by $CoMn_2O_4$, K-OMS-2, and Cu-BTC, respectively, after 3 regeneration cycles.

3.7 Oxidation studies of asphaltenes adsorbed onto the prepared nanocomposites

Catalytic oxidation studies of asphaltenes were conducted to determine the performance of the prepared nanocomposites in lowering the oxidation temperature of asphaltenes. The studies were performed in a TGA, and the thermal degradation profile was obtained for asphaltenes, Cu-BTC, asphaltene–Cu-BTC, asphaltene–$CoMn_2O_4$, and asphaltene–K-OMS-2 systems, as shown in Fig. 8.[88] All analyses were performed in an air atmosphere with the temperature ramped from 50 °C to 700 °C at a heating rate of 10 °C min^{-1}.[89] The thermal degradation of asphaltenes and Cu-BTC was investigated directly, while the catalytic degradation of asphaltenes was studied by subjecting equal-mass mixtures of each nanocomposite and asphaltene. From the figure, the oxidation of the asphaltenes was observed at about 600 °C and the degradation trend plateaus at 0 weight% after 600 °C. The trend indicates the complete oxidation of the asphaltenes above 600 °C without the formation of residual mass.

Fig. 8 illustrates the oxidation profiles of asphaltenes in the presence of the nanocomposites. From the figure, the Cu-BTC-catalysed asphaltene oxidation was observed at 540 °C, indicating a reduction in oxidation temperature, in comparison with non-catalysed oxidation. In addition, a 20% residual mass was observed which revealed the decomposition of the MOF, given

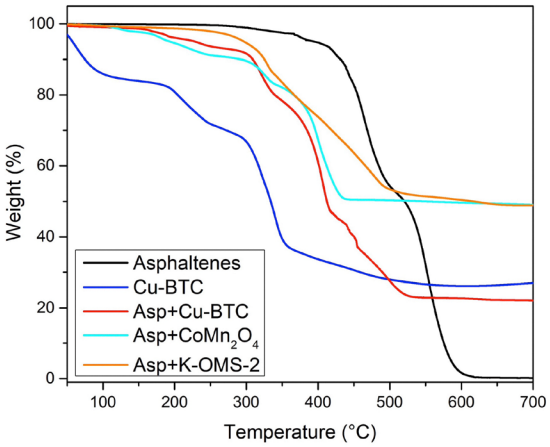

Fig. 8 Thermal degradation profile of Cu-BTC, asphaltenes, and asphaltenes subjected to oxidation under Cu-BTC, $CoMn_2O_4$, and K-OMS-2.

that equal mass ratios were used in the analysis. To further investigate the oxidation phenomenon, the thermal degradation analysis of Cu-BTC was performed. The thermal degradation profile along with a previous study involving MOFs, confirmed the decomposition of Cu-BTC and the formation of metal oxides well before the asphaltene oxidation temperature.[53] These observations demonstrate that Cu-BTC aids in asphaltene oxidation indirectly *via* its oxidation product, which acts as a catalyst. The metal oxide formed from Cu-BTC contributes to a 60 °C reduction in asphaltenes oxidation temperature.

Similarly, $CoMn_2O_4$ was studied for asphaltene oxidation. The thermal degradation profile showed a reduction in oxidation temperature from 600 °C to 440 °C. The stability of $CoMn_2O_4$ was also confirmed as the thermal profile remained unchanged above 440 °C, which was indicated by the horizontal trendline. Additionally, K-OMS-2 was studied for its capability in asphaltene oxidation, and the results indicated that K-OMS-2 reduced the oxidation temperature to 500 °C, showing its potential for regeneration. In both cases of asphaltene oxidation, the residual mass was observed to be about 50%, indicating complete oxidation of asphaltenes and the thermal stability of the nanocomposites. The thermal stability of the nanocomposites can be attributed to the high-temperature calcination step involved in the synthesis. However, K-OMS-2's high adsorption capacity, due to its tunnel-like pores and surface functional groups, did not significantly enhance oxidation, possibly due to the inefficiency of Mn phase formation during oxidation. These observations suggest that the catalytic oxidation capabilities of K-OMS-2 are limited, while it remains an efficient adsorbent.[46,47] Meanwhile, the presence of basic sites enhances the catalytic activity of the materials; hence, $CoMn_2O_4$ outperformed Cu-BTC and K-OMS-2 in catalytic oxidation of asphaltenes.[74]

3.8 Cost analysis of the adsorbent

The operational cost of the adsorption process is a critical factor that distinguishes it from other separation techniques. This operational cost is primarily determined by the expenses

associated with adsorbent preparation. To evaluate the feasibility of the process, a cost estimation was conducted based on the synthesis of 1 kg of adsorbent. The total cost includes raw materials, heating, drying, transportation, and electricity consumption during the synthesis process. The total cost estimate of the prepared nanocomposites is as follows:

- Cu-BTC: precursors (copper nitrate, BTC, DMF, and ethanol) cost = INR 16 300 kg^{-1}. Total production cost = INR 16 500 kg^{-1}.
- $CoMn_2O_4$: precursors (cobalt nitrate, manganese nitrate, ammonium hydroxide) cost = INR 3080 kg^{-1}. Total production cost = INR 3150 kg^{-1}.
- K-OMS-2: precursors (potassium permanganate, manganese sulphate, nitric acid) cost = INR 730 kg^{-1}. Total production cost = INR 780 kg^{-1}.

K-OMS-2 emerged as the most cost-effective material, offering the highest adsorption capacity (245.79 mg g^{-1}) at the lowest expense.

3.9 Environmental impact of the study

The nanocomposites were synthesised using cost-effective, readily available precursors without heavy metals. The synthesis techniques such as solvothermal synthesis, co-precipitation, and reflux boiling are simple and scalable. While hazardous DMF in MOF purification raises environmental concerns, substituting it with ethanol offers a greener alternative. The high-temperature calcination required for mixed metal oxides/OMS formation is the sole energy-intensive step. Additionally, *n*-heptane used in asphaltene extraction poses an environmental hazard, and hence, it is reused *via* distillation (Section 2.4).

Adsorption of asphaltenes significantly reduces energy consumption, resource use, and costs associated with asphaltene-related problems. Asphaltenes contribute to significant financial expenditure and pollution. This study provides a cost-effective, environmentally safe method for their removal. It also addresses the secondary environmental pollution that arises from disposal of spent adsorbents. The nanocomposites can generally be reused over multiple adsorption–desorption cycles as detailed in the reusability studies section. This approach also enables asphaltene recovery and utilisation. Furthermore, regeneration of the saturated adsorbents is also studied in the oxidation studies, which emphasises the reusability of the adsorbent. However, regeneration of the MOF is impractical due to framework decomposition at high temperatures, converting them into metal oxides. These oxides retain utility for alternative applications, enabling secondary material reuse.[53,90]

4. Conclusions

This study investigated the adsorption of petroleum residues (asphaltenes) using three adsorbents: Cu-BTC (metal–organic framework), $CoMn_2O_4$ (spinel oxide), and K-OMS-2 (octahedral molecular sieve). Asphaltenes, being the heaviest and most polar fraction of crude oil with limited practical applications, were effectively adsorbed by all the prepared materials, demonstrating maximum adsorption capacity q_m of 245 mg g^{-1} for K-OMS-2. The adsorption studies revealed the following for the prepared adsorbents:

- Cu-BTC followed the Freundlich isotherm, indicating multilayer adsorption, with kinetic and thermodynamic studies suggesting physisorption dominance.
- $CoMn_2O_4$ adhered to the Langmuir isotherm (monolayer adsorption) and exhibited chemisorption behaviour.
- K-OMS-2 aligned with the Hill isotherm, reflecting cooperative adsorption, alongside chemisorption kinetics.

Intraparticle diffusion models revealed a multi-step adsorption process across all systems, with Boyd plots confirming film diffusion as the rate-limiting step. Regeneration studies revealed the decomposition of Cu-BTC below the asphaltene oxidation temperature rendering it unsuitable for reuse. $CoMn_2O_4$ and K-OMS-2 retained structural integrity, with $CoMn_2O_4$ showing particularly efficient regeneration due to thermal stability. These results highlight the exceptional adsorption performance of K-OMS-2 and superior catalytic capabilities of $CoMn_2O_4$, which makes them promising materials for industrial asphaltene management. However, studies using isolated asphaltenes may not yield the real behaviour of petroleum residues, since asphaltenes are specific to their source and crude oil contains a number of other polyaromatic species that can interfere in real-time samples. Hence, future work should investigate interactions with additional polyaromatic species under real-time conditions, and be expanded to include asphaltenes from diverse geological sources, given their composition-dependent behaviour.

Author contributions

Abhishek Nayak: conceptualisation, methodology, investigation, data curation, validation, visualisation, formal analysis, and writing – original draft. Shanon Viegas and Adrian Marcel Rodrigues: methodology, investigation, data curation, and formal analysis. Nithya Rajagopal: conceptualisation, methodology, validation, visualisation, and formal analysis. Harshini Dasari and Nethaji Sundarabal: supervision, funding acquisition, project administration, and writing – review & editing.

Conflicts of interest

There are no conflicts to declare.

Data availability

Data for this article are available in the manuscript and ESI.†

Acknowledgements

The authors would like to acknowledge the financial support given by Vision Group on Science and Technology (VGST), Govt. of Karnataka, India and Manipal Research Board (MRB), Manipal Academy of Higher Education (MAHE),

Manipal, India. The authors would also like to thank SCIF, SRMIST, and CRF, NITK for providing the instrumentation facilities.

References

1 H. S. Jung and N. G. Park, *Small*, 2015, **11**, 10–25.
2 H. Groenzin and O. C. Mullins, in *Asphaltene Molecular Size and Weight by Time-Resolved Fluorescence Depolarization*, ed. O. C. Mullins, E. Y. Sheu, A. Hammami and A. G. Marshall, Springer New York, New York, NY, 2007, pp. 17–62.
3 I. Mohammed, M. Mahmoud, D. Al Shehri, A. El Husseiny and O. Alade, *J. Pet. Sci. Eng.*, 2021, **197**, 107956.
4 S. M. Anisuzzaman and R. Karali, *AIP Conf. Proc.*, 2023, **2945**, 020004.
5 K. Ahmad, *et al.*, *J. Cleaner Prod.*, 2023, **388**, 136014.
6 E. Buenrostro Gonzalez, S. I. Andersen, J. A. Garcia Martinez and C. Lira Galeana, *Energy Fuels*, 2002, **16**, 732–741.
7 F. Mansoori Mosleh, Y. Mortazavi, N. Hosseinpour and A. A. Khodadadi, *Energy Fuels*, 2019, **34**, 211–224.
8 H. L. Girard, P. Bourrianne, D. Chen, A. Jaishankar, J. L. Vreeland, R. E. Cohen, K. K. Varanasi and G. H. McKinley, *Langmuir*, 2020, **36**, 3894–3902.
9 N. Setoodeh, P. Darvishi and A. Lashanizadegan, *J. Dispersion Sci. Technol.*, 2018, **39**, 452–459.
10 T. Guo, M. S. Yao, Y. H. Lin and C. W. Nan, *CrystEngComm*, 2015, **17**, 3551–3585.
11 D. Jiang, M. Chen, H. Wang, G. Zeng, D. Huang, M. Cheng, Y. Liu, W. Xue and Z. Wang, *Coord. Chem. Rev.*, 2019, **380**, 471–483.
12 J. Ling, A. Zhou, W. Wang, X. Jia, M. Ma and Y. Li, *ACS Omega*, 2022, **7**, 19920–19929.
13 Y. Belmabkhout, P. M. Bhatt, K. Adil, R. S. Pillai, A. Cadiau, A. Shkurenko, G. Maurin, G. Liu, W. J. Koros and M. Eddaoudi, *Nat. Energy*, 2018, **3**, 1059–1066.
14 F. Chen, D. Lai, L. Guo, J. Wang, P. Zhang, K. Wu, Z. Zhang, Q. Yang, Y. Yang and B. Chen, *et al.*, *J. Am. Chem. Soc.*, 2021, **143**, 9040–9047.
15 X. Zhang, R.-B. Lin, Z. A. Alothman, O. Alduhaish, T. Yildirim, W. Zhou, J.-R. Li and B. Chen, *Inorg. Chem. Front.*, 2023, **10**, 454–459.
16 Z. Bao, L. Yu, Q. Ren, X. Lu and S. Deng, *J. Colloid Interface Sci.*, 2011, **353**, 549–556.
17 L. Guo, J. Hurd, M. He, W. Lu, J. Li, D. Crawshaw, M. Fan, S. Sapchenko, Y. Chen and X. Zeng, *et al.*, *Commun. Chem.*, 2023, **6**, 55.
18 A. A. Adeyemo, I. O. Adeoye and O. S. Bello, *Toxicol. Environ. Chem.*, 2012, **94**, 1846–1863.
19 C. Wang, C. Xiong, Y. He, C. Yang, X. Li, J. Zheng and S. Wang, *Chem. Eng. J.*, 2021, **415**, 128923.
20 B. Valizadeh, T. N. Nguyen, S. Kampouri, D. T. Sun, M. D. Mensi, K. Stylianou, B. Smit and W. L. Queen, *J. Phys. Chem. C*, 2020, **8**, 9629–9637.
21 D. Pan, S. Ge, J. Zhao, Q. Shao, L. Guo, X. Zhang, J. Lin, G. Xu and Z. Guo, *Dalton Trans.*, 2018, **47**, 9765–9778.
22 I. Ahmad, S. H. Serbaya, A. Rizwan and M. S. Mehmood, *J. Spectrosc.*, 2021, **2021**, 6629640.
23 S. E. Haggerty, *Opaque Mineral Oxides in Terrestrial Igneous Rocks*, De Gruyter, Berlin, Boston, 1976, ch. 8, pp. 303–502.
24 L. Shu, J. Sunarso, S. S. Hashim, J. Mao, W. Zhou and F. Liang, *Int. J. Hydrogen Energy*, 2019, **44**, 31275–31304.
25 R. Li, Y. Li and Z. Liu, *Fuel*, 2024, **355**, 129405.
26 K. K. Kefeni, B. B. Mamba and T. A. Msagati, *Sep. Purif. Technol.*, 2017, **188**, 399–422.
27 V. V. Halali, C. Sanjayan, V. Suvina, M. Sakar and R. G. Balakrishna, *et al.*, *Inorg. Chem. Front.*, 2020, **7**, 2702–2725.
28 P. Tan, M. Liu, Z. Shao and M. Ni, *Adv. Energy Mater.*, 2017, **7**, 1602674.
29 K. Jin, G. He, X. Zhang, S. Maruyama, S. Yasui, R. Suchoski, J. Shin, Y. Jiang, H. Yu and J. Yuan, *et al.*, *Nat. Commun.*, 2015, **6**, 7183.
30 S. K. Chang, Z. Zainal, K. B. Tan, N. A. Yusof, W. M. D. W. Yusoff and S. Prabaharan, *Ceram. Int.*, 2015, **41**, 1–14.
31 R. Suresh, S. Rajendran, P. S. Kumar, D. V. N. Vo and L. Cornejo Ponce, *Chemosphere*, 2021, **274**, 129734.
32 C. Shan, Y. Wang, J. Li, Q. Zhao, R. Han, C. Liu and Q. Liu, *Environ. Sci. Technol.*, 2023, **57**, 9495–9514.
33 K. Cai, S.-H. Luo, J. Feng, J. Wang, Y. Zhan, Q. Wang, Y. Zhang and X. Liu, *Chem. Rec.*, 2022, **22**, e202100169.
34 H. Xu, J. Yuan, G. He and H. Chen, *Coord. Chem. Rev.*, 2023, **475**, 214869.
35 K. R. Sanchez Lievanos, T. Sun, E. A. Gendrich and K. E. Knowles, *Chem. Mater.*, 2024, **36**, 3981–3998.
36 S. Sobhanardakani and R. Zandipak, *Sep. Sci. Technol.*, 2018, **53**, 2339–2351.
37 F. Di Quarto, A. Zaffora, F. Di Franco and M. Santamaria, *ACS Org. Inorg. Au*, 2023, **4**, 120–134.
38 M. Liu, Z. Rong, R. Malik, P. Canepa, A. Jain, G. Ceder and K. A. Persson, *Energy Environ. Sci.*, 2015, **8**, 964–974.
39 L. Zhang, X. Bi, M. Gou, M. Sun, L. Tao, G. Chen, X. Liu, X. Meng and P. Zhao, *Sep. Purif. Technol.*, 2021, **263**, 118397.
40 F. M. Kalimani and A. Khorshidi, *RSC Adv.*, 2023, **13**, 6909–6918.
41 H. Wang, M. Wang, X. Liang, J. Yuan, H. Yang, S. Wang, Y. Ren, H. Wu, F. Pan and Z. Jiang, *Chem. Soc. Rev.*, 2021, **50**, 5468–5516.
42 R. M. Martn Aranda and J. Čejka, *Top. Catal.*, 2010, **53**, 141–153.
43 X. Shen, X. Du, D. Yang, J. Ran, Z. Yang and Y. Chen, *J. Environ. Chem. Eng.*, 2021, **9**, 106729.
44 F. Sabaté and M. J. Sabater, *Catalysts*, 2021, **11**, 1147.
45 F. M. Kalimani and A. Khorshidi, *RSC Adv.*, 2023, **13**, 6909–6918.
46 J. Hou, L. Liu, Y. Li, M. Mao, H. Lv and X. Zhao, *Environ. Sci. Technol.*, 2013, **47**, 13730–13736.
47 X. Zhang, Z. Ma, Z. Song, H. Zhao, W. Liu, M. Zhao and J. Zhao, *J. Phys. Chem. C*, 2019, **123**, 17255–17264.
48 N. Garg, M. Mishra and A. K. Ganguli, *et al.*, *RSC Adv.*, 2015, **5**, 84988–84998.
49 W. A. El Yazeed and A. I. Ahmed, *RSC Adv.*, 2019, **9**, 18803–18813.

50 L. Zhou, D. Zhao and X. W. Lou, *Adv. Mater.*, 2012, **24**, 745–748.
51 P. H. Ho, S. C. Lee, J. Kim, D. Lee and H. C. Woo, *Fuel Process. Technol.*, 2015, **131**, 238–246.
52 F. Soorghali, A. Zolghadr and S. Ayatollahi, *Energy Fuels*, 2014, **28**, 2415–2421.
53 A. Nayak, S. Viegas, H. Dasari and N. Sundarabal, *ACS Omega*, 2022, **7**, 34966–34973.
54 H. Alboudwarej, D. Pole, W. Y. Svrcek and H. W. Yarranton, *Ind. Eng. Chem. Res.*, 2005, **44**, 5585–5592.
55 M. S. Mazloom, A. Hemmati Sarapardeh, M. M. Husein, H. S. Behbahani and S. Zendehboudi, *Fuel*, 2020, **279**, 117763.
56 J. Cheng, X. Xuan, X. Yang, J. Zhou and K. Cen, *RSC Adv.*, 2018, **8**, 32296–32303.
57 R. Kaur, A. Kaur, A. Umar, W. A. Anderson and S. K. Kansal, *Mater. Res. Bull.*, 2019, **109**, 124–133.
58 Z. Liu and H. Li, *Energy Environ. Mater.*, 2023, **6**, e12255.
59 T. A. Sandosh and A. Simi, *Chem. Pap.*, 2021, **75**, 2295–2304.
60 H.-B. Luo, H.-D. Mao, Q. Chen, R. Zhang, Y.-H. Qin, Z. Chen, L. Yang and C.-W. Wang, *Ind. Eng. Chem. Res.*, 2024, **63**, 4297–4305.
61 H. M. Galindo, Y. Carvajal, E. Njagi, R. A. Ristau and S. L. Suib, *Langmuir*, 2010, **26**, 13677–13683.
62 R. Nivetha, A. Sajeev, A. M. Paul, K. Gothandapani, S. Gnanasekar, P. Bhardwaj, G. Jacob, R. Sellappan, V. Raghavan and S. Pitchaimuthu, *et al.*, *Mater. Res. Express*, 2020, **7**, 114001.
63 Y. Gao, D. R. Kong, Z. Y. Zhang, X. F. Zhang, Z. P. Deng, L. H. Huo and S. Gao, *J. Alloys Compd.*, 2022, **897**, 163158.
64 I. Kihal, S. Douafer, H. Lahmar, G. Rekhila, S. Hcini, M. Trari and M. Benamira, *J. Photochem. Photobiol., A*, 2024, **446**, 115170.
65 E. M. Kalhori, E. Ghahramani, T. J. Al Musawi, H. N. Saleh, M. N. Sepehr and M. Zarrabi, *Environ. Sci. Pollut. Res.*, 2018, **25**, 34164–34180.
66 Y. Li, Y. Li, Q. Shi, M. Qiu and S. Zhan, *J. Sol-Gel Sci. Technol.*, 2017, **81**, 576–585.
67 J. Zhao, B. Jin and R. Peng, *Nanoscale Adv.*, 2020, **2**, 5682–5687.
68 H. Wu, W. Lu, Y. Chen, P. Zhang and X. Cheng, *Energy Fuels*, 2020, **34**, 7363–7372.
69 A. Biswas and C. Prathibha, *Mater. Adv.*, 2022, **3**, 5947–5963.
70 X. Zhou, R. Maimaitiniyazi and Y. Wang, *Arabian J. Chem.*, 2022, **15**, 104267.
71 H. N. Tran, N. P. Thanh Trung, E. C. Lima, J.-C. Bollinger, N. D. Dat, H.-P. Chao and R.-S. Juang, *J. Chem. Technol. Biotechnol.*, 2023, **98**, 462–472.
72 G. K. Rajahmundry, C. Garlapati, P. S. Kumar, R. S. Alwi and D.-V. N. Vo, *Chemosphere*, 2021, **276**, 130176.
73 R. Saadi, Z. Saadi, R. Fazaeli and N. E. Fard, *Korean J. Chem. Eng.*, 2015, **32**, 787–799.
74 N. N. Nassar, A. Hassan and P. Pereira Almao, *J. Colloid Interface Sci.*, 2011, **360**, 233–238.
75 H. Moussout, H. Ahlafi, M. Aazza and H. Maghat, *Karbala Int. J. Mod. Sci.*, 2018, **4**, 244–254.
76 L. Largitte and R. Pasquier, *Chem. Eng. Res. Des.*, 2016, **109**, 495–504.
77 N. A. Rashidi, A. Bokhari and S. Yusup, *Environ. Sci. Pollut. Res.*, 2021, **28**, 33967–33979.
78 A. Inyinbor, F. Adekola and G. A. Olatunji, *Water Resour. Ind.*, 2016, **15**, 14–27.
79 M. Madhi, A. Bemani, A. Daryasafar and M. R. Khosravi Nikou, *Pet. Sci. Technol.*, 2017, **35**, 242–248.
80 D. Sarkar, S. Ganguli, A. E. Praveen and V. Mahalingam, *Mater. Adv.*, 2020, **1**, 2019–2032.
81 N. Mironov, D. Milordov, E. Tazeeva, D. Tazeev, G. Abilova, S. Yakubova and M. Yakubov, *Energy Fuels*, 2021, **35**, 14527–14541.
82 Z. Hosseini Dastgerdi and S. S. Meshkat, *J. Pet. Sci. Eng.*, 2019, **174**, 1053–1061.
83 M. P. Tavlieva, S. D. Genieva, V. G. Georgieva and L. T. Vlaev, *J. Colloid Interface Sci.*, 2013, **409**, 112–122.
84 P. S. Ghosal and A. K. Gupta, *J. Mol. Liq.*, 2017, **225**, 137–146.
85 C. Franco, E. Patiño, P. Benjumea, M. A. Ruiz and F. B. Cortés, *Fuel*, 2013, **105**, 408–414.
86 J. Piccin, G. Dotto and L. Pinto, *Braz. J. Chem. Eng.*, 2011, **28**, 295–304.
87 L. Tapio, S. Subramanian, S. Simon and J. Sjöblom, *J. Dispersion Sci. Technol.*, 2017, **38**, 355–360.
88 N. N. Nassar, A. Hassan, L. Carbognani, F. L. Linares and P. Pereira Almao, *Fuel*, 2012, **95**, 257–262.
89 N. N. Nassar, A. Hassan and P. Pereira Almao, *Colloids Surf., A*, 2011, **384**, 145–149.
90 N. Rajagopal, H. P. Uppara, H. Dasari, V. C. S. Palla and S. R. Yenumala, *Inorg. Chem. Commun.*, 2023, **155**, 111126.